A Natural 3D Interconnected Laminated Composite with Enhanced Damage Resistance

Ling Li and Christine Ortiz**

Due to their lightweight, high specific stiffness and strength, cost effectiveness, corrosion and fatigue resistance, laminated composites have been widely used in many engineering applications, such as aircraft, automobiles, sporting products, and civil infrastructure. However, delamination damage along in-plane interfaces has been one of the issues that still remain unsolved. Although many natural load-bearing materials are also essentially laminated composites composed of mineral and organic phases, the underlying mechanisms for antidelamination are still largely unexplored. Here it is reported that the remarkable resistance to macroscopic indentation damage in the highly mineralized shell of the bivalve *Placuna placenta* originates from a characteristic nanoscale structural motif, i.e., screw dislocation-like connection centers, which join adjacent mineral layers together in the laminate structure. This leads to the formation of a complex interconnected network of microcracks surrounding the damage zone, which allows for both efficient energy dissipation and damage localization even when the shell is completely penetrated. Both theoretical analysis and experiment-based calculations suggest that the interfacial fracture toughness is enhanced by almost two orders of magnitude in comparison to classic laminated composites without connection centers. This design strategy for achieving a 3D integrative laminate architecture can be potentially applied in the design of advanced laminated composite materials.

1. Introduction

High strength and toughness, perhaps the two most important mechanical properties, are unfortunately almost always mutually exclusive in monolithic materials.[1,2] Scientists have long recognized that by combining multiple materials with complementary properties, one can make structural materials with unusual combination of mechanical properties.[3] In the past few decades, there has been significant progress in developing high-performance composite materials, such as carbon and aramide fiber–based composites.[3,4] In particular, laminated composite materials based on these high-strength reinforcing fibers have been among the most widely used composite materials due to their cost effectiveness, lightweight, and high axial strength.[3,4] However, several drawbacks of these composites remain unresolved, including in-plane delamination[4] and low damage resistance against out-of-plane impact,[3–5] despite some demonstrated improvements through approaches such as placing out-of-plane fibers,[6–8] 3D weaving,[9,10] or growing aligned carbon nanotubes on the surface of the reinforcing fiber.[11]

Natural load-bearing materials, such as mollusk shells, fish scales, arthropod exoskeletons, bones, and sponge spicules, are almost exclusively composites made with both strong/brittle mineral and soft/weak organic phases.[12–14] Despite the tremendous constraints in material selections, many biological species have developed, through million years of evolution, effective ways of enhancing the mechanical properties of their composites beyond the rule of mixture.[1,12,15] Interestingly, composites with laminate configurations are one of the most commonly found structural motifs in these biological materials.[16–18] For example, the laminated structure of nacre is able to enhance toughness by orders of magnitude as compared to its primary constituent, aragonite, while still maintaining high strength and modulus.[19–22] Study of the underlying structural characteristics that allow for amplified mechanical properties in these natural laminated composites could generate effective design strategies for advanced laminate-based engineering composite materials.[13,14,23–29]

Recently, we discovered that the shells of the bivalve *Placuna placenta*, despite their very high mineral content (≈99 wt% of calcite), are able to localize microscopic indentation damage and enhance energy dissipation by almost an order of magnitude relative to single crystal calcite.[30,31] The fundamental mechanisms responsible for such a remarkable improvement lies in the shell's laminated structure of nanoscopic calcitic layers. This structure generates extensive deformation twinning and other deformation modes (such as interface opening, stretching of organics, fragmentation, nano-/microcracking, etc.) around the indentation site, which localizes damage and allows for efficient energy dissipation.[31]

Here, we explore the hierarchical macroscale structural origins of the excellent damage tolerance and multihit capability of this natural laminated composite. A characteristic nanoscale structural motif, i.e., screw dislocation-like connection centers,

Dr. L. Li,[+] Prof. C. Ortiz
Department of Materials Science and Engineering
Massachusetts Institute of Technology
77 Massachusetts Avenue, Cambridge, MA 02139, USA
E-mail: lingli@seas.harvard.edu; cortiz@mit.edu
[+]Present address: School of Engineering and Applied Sciences, Harvard University, 9 Oxford Street, Cambridge, MA 02138, USA

DOI: 10.1002/adfm.201500380

joins adjacent mineral layers together. Similar screw dislocation-like structures have been previously observed in nacreous shells.[32–34] They are believed primarily to provide a biomineralization pathway for the formation of the nacreous structure through the spiral growth mechanism.[32–34] A recent study by Yao et al. suggested that the connection centers in nacre might also enhance its strength by interlocking and resisting tablets' motion.[33] In this work, by using electron microscopic imaging over large areas (>5 mm^2) we present a detailed quantitative analysis of the handiness, distribution, density, and association characteristics of these connection centers. This analysis led us to hypothesize that the shell of *P. placenta* has, instead of a classic 2D laminated structure with separated layers, a 3D integrated and interconnected laminated structure in which all the mineral layers are joined together by connection centers. Macroscopic deformation behavior was investigated through a customized macroindentation technique with loads high enough to penetrate intact shells. Through high-resolution synchrotron X-ray micro-computed tomography (μ-CT), we found that the shell is able to localize damage even if it is entirely penetrated. This technique also revealed that a complex interconnected network of microcracks is formed within the localized damage zone. Combining these results with electron microscopy, we show that the connection centers act as anchoring centers for the formation of bridging ligament, which resist crack opening behind crack tips and retard crack propagation. In addition, we determined that microscopic plastic deformation mechanisms are initiated in the vicinity of connection centers. Experiment-based calculations and a theoretical analysis reveal that this microscopic plasticity enhances the interfacial fracture toughness by almost two orders of magnitude as compared to classic 2D laminated composites.

2. Results

2.1. Screw Dislocation-Like Connection Centers

P. placenta shell is a highly mineralized (≈99 wt%) calcite-based laminated composite.[30] The structure consists of elongated diamond-shaped calcitic laths (length, ≈140 μm; width, ≈6 μm). The thickness of the mineral and organic layers are ≈300 and ≈1–2 nm, respectively.[30] However, careful examination of fractured surfaces of the shells revealed a hidden special microstructural feature, through which an underlying mineral layer is connected to the layer above, similar to the way two adjacent atomic planes are connected through a screw dislocation (**Figure 1**). These screw dislocation-like connection centers have two opposite signs, i.e., up and down (according to the right-hand rule), as shown in Figure 1a. The height image measured from atomic force microscopy (AFM) further revealed that the merged mineral layer gradually increases the layer thickness to the nominal values (≈300 nm) over a distance of ≈3 μm from the center of connections. This leads to inclination angles in the transition regions of ≈3°. The presence of connection centers can also be visualized through polished cross-sectional surface (Figure 1c), where extra interfaces (white arrows) are associated with insertion of additional mineral layers via connection centers.

The distribution of connection centers was investigated by mapping fracture surfaces over large areas using scanning electron microscopic (SEM) imaging. The samples were prepared by carefully cleaving along the interfacial orientation of the shell using a razor blade, which could suppress microscopic damages at mineral layers. This type of "clean" fracture surfaces, in contrast to those with microscopic damages (as discussed later), were selected for quantitative measurement of the distribution of connection centers because it is easier to identify their positions. As shown in a representative region in Figure 1d, we first traced the fracture lines of individual mineral layers after the shell was fractured along the interface direction (Figure S1, Supporting Information). The connection centers were then identified and marked with signs (Figure 1d and Figure S2, Supporting Information). Two parameters are defined: d, the distance between two associated connection centers with opposite signs, which are connected with a common fracture line; λ, the spacing between two adjacent fracture lines. Figure 1e depicts a typical large-area (≈5.7 mm^2) distribution of connection centers, which consists of 483 down-signed and 504 up-signed connection centers, respectively. Both types of connection centers are roughly uniformly distributed within the analyzed region (areal density, ρ_{area}, 100–400 mm^{-2}), although there are slight local variations.

Figure 1f shows the full fracture lines ended with two associated connection centers with opposite signs within the analyzed region, and Figure 1g plots the statistical distribution of their lengths (d). The distribution can be well fitted with a logarithmic distribution. 55.9% of the measured distances d are below 0.5 mm, and the number average is 574 ± 509 μm (n = 270). Here, we should point out that this statistical distribution of d might be skewed toward the lower end, as long fracture lines, which were not completely located within the analyzed region, were not counted in this statistical measurement.

Through a simple geometrical model as described in Figure S3 (Supporting Information), the volumetric density of connection centers, ρ_{volume}, is estimated to be $1.7–6.7 \times 10^5$ mm^{-3}, using the experimentally measured areal density (ρ_{area}, 100–400 mm^{-2}). The total volume of a typical *P. placenta* shell is about 4×10^3 mm^3 (thickness, ≈0.5 mm; diameter, ≈10 cm). Thus, the total number of connection centers within the entire shell can then be estimated as $\approx 2 \times 10^9$, which corresponds to $\approx 10^6$ connection centers distributed within each mineral layer (≈2000 layers throughout the entire shell). Based on the large-area structural analysis and the experiment-based calculations, we hypothesize that the microstructure of *P. placenta* shell has, instead of a simple laminated structure with separated mineral layers, an integrated 3D composite laminated structure, where all the mineral layers are connected together through these screw dislocation-like connection centers.

Moreover, since the connection centers directly induce the formation of the fracture lines, the number of fracture lines within an area should be directly proportional to the density of connection centers. Therefore, we have

$$\rho_{area} \propto \frac{1}{\lambda} \tag{1}$$

This inverse relationship is supported by the linear fit between ρ_{area} and $1/\lambda$ with the slope of 6.1 ± 1.3 mm^{-1} (Figure 1h).

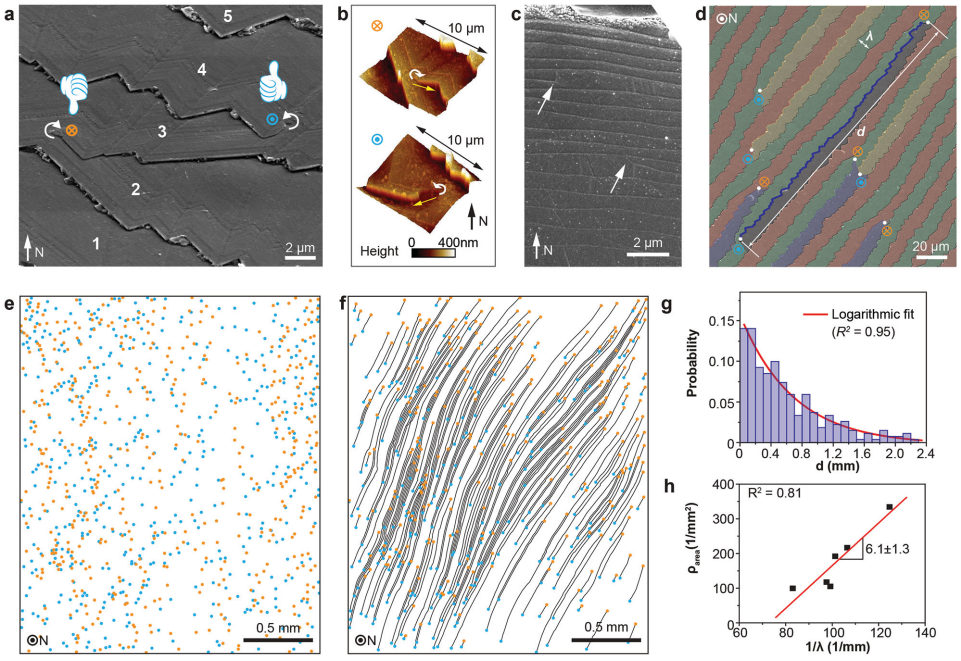

Figure 1. Screw dislocation-like connection centers in the laminated structure of *P. placenta* shells. a) SEM image showing two connection centers with opposite signs in a fracture surface. Individual mineral layers are labeled from 1 to 5. The signs of connection centers (up and down) are defined according to the right-hand rule: with fingers pointing along the direction from the bottom to the adjacent top layer, the direction of thumb determines the sign of the connection center. The blue and orange markers indicate the up- and down-signed connection centers, respectively. b) AFM height image of two connection centers with opposite signs. The thickness of mineral layers gradually increases to the nominal values (≈300 nm) over a distance ≈3 μm from the center of connections (along the yellow arrows). c) SEM image of a polished cross section showing two half-ended interfaces (indicated by white arrows), which are due to the presence of additional mineral layers resulted from connection centers. d) SEM image of a fractured interface, from which fracture lines and connection centers are traced and marked, respectively. The image is artificially colored to further highlight individual mineral layers. Two parameters are defined: λ, the distance between two adjacent fractured lines; d, the distance between two associated connection centers with opposite signs. e) Large-area mapping of connection centers, and f) the corresponding image of the full fracture lines ended with two connection centers with opposite signs. g) Distribution of the distance between two associated connection centers, d. The red line represents a logarithmic fit ($p = p_0 + Ae^{Rod}$). h) The areal density of connection centers (ρ_{area}) as a function of the inverse of the fracture line spacing ($1/\lambda$).

2.2. Macroscopic Damage Resistance

We next investigated the mechanical behavior of *P. placenta* shells at large length scales to establish its relationship to the structural features discussed above. Intact shells were tested through a customized indentation instrument with high load capabilities, through which an entire shell can be penetrated by a tungsten indentation tip (Experimental Section, **Figure 2**a,b). The as-obtained load-depth curves reveal two regimes (Figure 2c):

Regime 1: As the indentation tip slowly indented into the shell, the load increased gradually to a maximum value (F_{max}) at which point the shell was fractured (a "breaking" sound could be clearly heard).

Regime 2: This is the postfracture penetration process during which the indentation tip continuously pushed out fractured shell pieces and penetrated deeper until the load dropped to approximately zero.

Upon complete penetration, the biological nanocomposite underwent extremely localized deformation (damage zone size, ≈2 mm) without any radial crack formation, enabling multihit capability within a small region (Figure 2d,e). For shells with thickness of 0.68 ± 0.03 mm, the maximum fracture loads were measured to be 64.6 ± 12.3 N (n = 7). Similar macroindentation experiments were also performed on calcite samples with similar thickness (red profiles in Figure 2c), which exhibited brittle catastrophic fracture behavior without any postfracture inelastic deformation. Moreover, the maximum fracture loads for calcite (17.8 ± 6.6 N; thickness, 0.76 ± 0.09 mm; n = 4) are much lower in comparison to *P. placenta*. The fractured pieces of calcite samples after indentation tests had little visible inelastic deformations close to the indentation site, and the fracture readily followed the easy cleavage planes of calcite (Figure 2f). The contribution of sample bending to the total displacement measured from this experiment was very small (≈0.5% of the total indentation depth) according to a simplified finite element simulation analysis and hence neglected (Figure S4, Supporting Information).

Thanks to the unique high optical transmission capability of the shell, the damage zone after indention can be directly visualized via optical microscopy in transmission mode (Figure 2d,e).[31] The decrease in optical transmittance in the damaged zone results from the disruption of the original intact densely packed structure and generation of interface openings, which causes light scattering and reduces transmission.

High-resolution synchrotron μ-CT was applied to investigate the microstructural characteristics within the damage zone in 3D (Experimental Section) to further explore the underlying deformation mechanisms behind such localized and isotropic

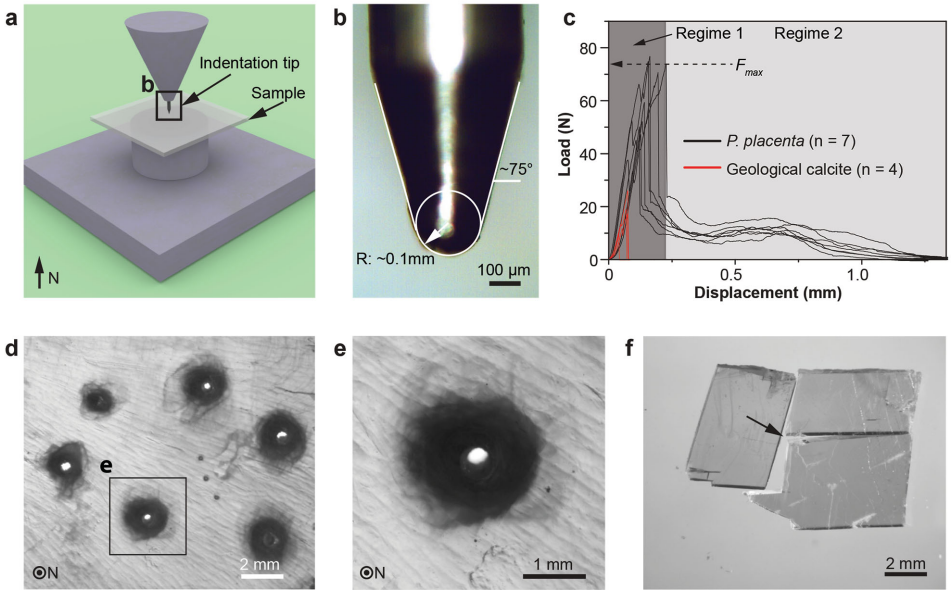

Figure 2. Macroscopic damage resistance of *P. placenta* shells through macroindentation tests. a) Schematic diagram of the experimental setup. The cylindrical steel substrate underneath the sample has a central hole (diameter, 5 mm) aligned with the indentation tip. b) Optical images of the tungsten indentation tip (full angle, ≈31°; tip radius, ≈0.1 mm). c) Representative macroindentation curves for *P. placenta* shells (thickness, 0.68 ± 0.03 mm; $n = 7$) and calcite (thickness, 0.76 ± 0.09 mm; $n = 4$). d) A *P. placenta* shell after multiple macroindentation tests with complete penetration. e) Optical image of one macroindentation residue in *P. placenta*, illustrating the isotropic localized damage (dark zone) surrounding the indentation site. f) Multiple pieces resulted from the brittle fracture of a calcite sample (thickness, ≈0.8 mm) after indentation test. The black arrow indicates the position of indention. Images in (d), (e), and (f) were taken in transmission mode. (d) and (e) are adapted from ref. [30].

damage (**Figure 3**). As shown in a typical 3D reconstruction (Figure 3a), the entire damage zone (dark region) resembles a conical frustum geometry (also seen in the 3D rendering movie in the Supporting Information). The diameter of the top penetration hole is ≈0.5 mm, close to the base diameter of the tungsten indentation tip. The diameter of the bottom of the damage zone is ≈2 mm, consistent with optical observations. A representative vertical slice of the indentation zone in Figure 3b reveals the formation of a complex interconnected network of microcracks. Moreover, the mineral layers close to the boundary of the damage zone have undergone shear failure with local breakages, and the resulted laminate orientation has rotated toward the indentation direction (yellow line in Figure 3b). Please note that the three large horizontal cracks seen in Figure 3b were generated during diamond saw cutting of the sample in order to fit it within the field of view of the X-ray beam. Figure 3c shows a series of horizontal slices of the damage zone. The corresponding locations of the slices are indicated by the red dashed lines in Figure 3b. These horizontal slices show that multiple microscopic cracks originating radially from the central indentation hole are enclosed by circumferential cracks, leading to the confined damage behavior.

Figure 3d,e shows 3D renderings of the microcrack network within the damage zone, corresponding to the vertical section shown in Figure 3a. Note that the surface mesh is a negative of the damage zone, i.e., it represents cracks between mineral layers. A large number of microcracks were formed surrounding the central indentation hole, and they branched and linked together to form a complex 3D interconnected network. This allows enhanced energy dissipation through increased interface opening within this confined volume. This complex interconnected network of microcracks maintains the structural integrity of the shell by reducing the possibility of large catastrophic interface failures. Moreover, the shear deformation of mineral layers, as revealed by the rotation of microcracks, results in a large amount of energy dissipation through local microscopic inelastic deformations (as discussed later).

We next provide direct experimental evidence for the formation of the interconnected microcrack network within the damage zone. As shown in a μ-CT cross section (**Figure 4**a), multiple ligaments connecting two opening surfaces were formed along a crack. A representative 3D reconstruction of such bridging ligament shown in Figure 4b further demonstrates that these bridges are able to hold the two fractured pieces together even with an interface opening greater than ≈50 μm.

Since the resolution of μ-CT imaging is approximately an order of magnitude larger than the thickness of individual mineral layers, direct analysis of such bridge structures at the individual layer level is not possible. Therefore, we conducted electron microscopic imaging of finely polished cross sections of damage zone to investigate this interface bridging mechanism at the building block level. Figure 4c,d shows an SEM image of a horizontal crack and a corresponding schematic diagram with individual mineral layers highlighted. In this example, the crack was originally propagating horizontally from left to right along an organic interface. After encountering the connection center by which the two mineral layers are joined, the crack was deflected to another interface on top, forming a bridging ligament between two interfaces. Through this mechanism, the materials at the two sides of a propagating crack can be bridged together, acting as a crack closure element.[1] We believe this is the primary mechanism responsible for forming the complex

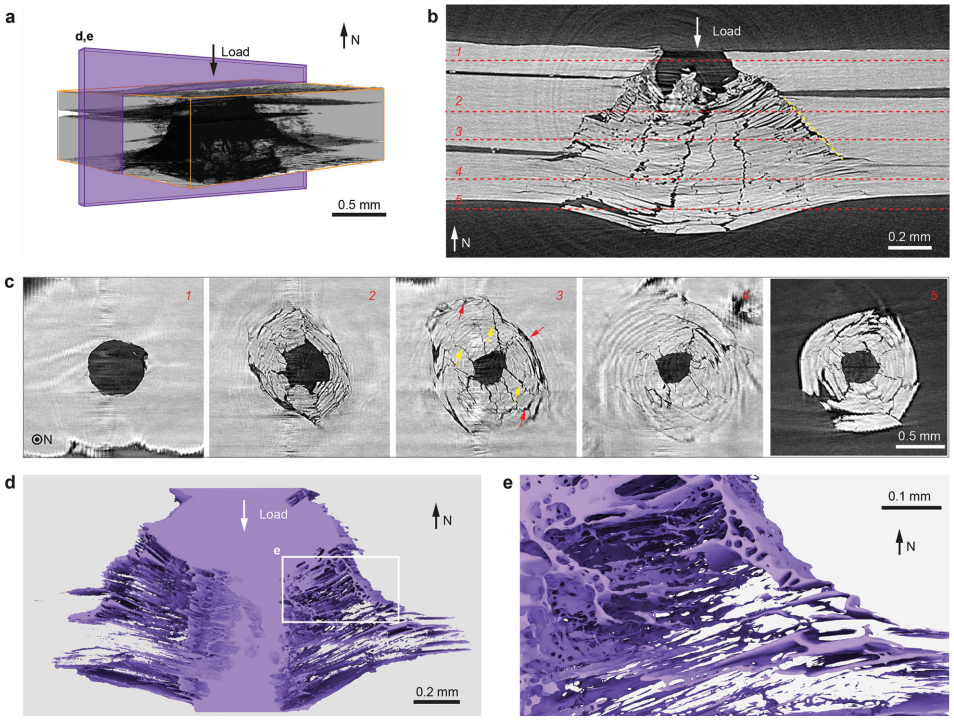

Figure 3. 3D analysis of the macroindentation damage zone via synchrotron micro-computed tomography (μ-CT). a) 3D reconstruction of the entire damage zone using a transparency effect. The central dark region with a conical frustum geometry indicates the localized damage. b) A vertical slice of the damage zone, illustrating the formation of the interconnected microcracks. The yellow dashed lines indicate the rotation of mineral layers close to the edge of the damage zone. c) Five horizontal μ-CT slices of the damage zone from top to the bottom of the damage zone, as indicated by the dashed lines 1–5 in (b). In slice 3, multiple microscopic cracks originating radially from the central indentation hole (yellow arrows) are enclosed by circumferential cracks (red arrows), leading to confined damage. d,e) 3D rendering of a vertical section of the damage zone using the negative effect, i.e., the reconstructed mesh surface is the microcracks generated by damage.

3D interconnected microcrack network within the damage zone, enabling both efficient energy dissipation and the ability to maintain structural integrity of the bioceramic armor under large penetration loads.

In addition to the formation of bridging ligaments, the presence of connection centers also directly activates deformation mechanisms at smaller length scales which are much more efficient at energy dissipation as compared to simple interface openings. As discussed in our previous work, *P. placenta* undergoes pervasive deformation twinning and other additional inelastic deformation mechanisms at nanoscale.[31] As shown by more commonly observed fracture surfaces in **Figure 5**a,b, a large number of microscopic inelastic deformations were observed along fracture lines, including deformation twinning,

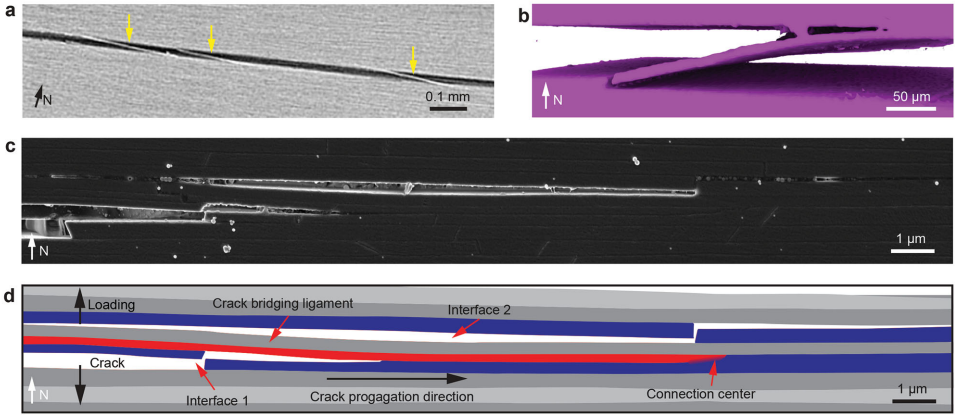

Figure 4. Crack bridging via connection centers. a) Vertical cross-sectional μ-CT image and b) a 3D reconstruction based on μ-CT data showing a bridging ligament formed along a crack. c) SEM image and d) corresponding schematic diagram showing the crack was deflected by the presence of a connection center. The "original crack" was propagating from the left to right along the "interface 1." After encountering the "connection center" ahead of the crack front, it was deflected to the "interface 2." Through this process, a "crack-bridging ligament" was formed between two cracks.

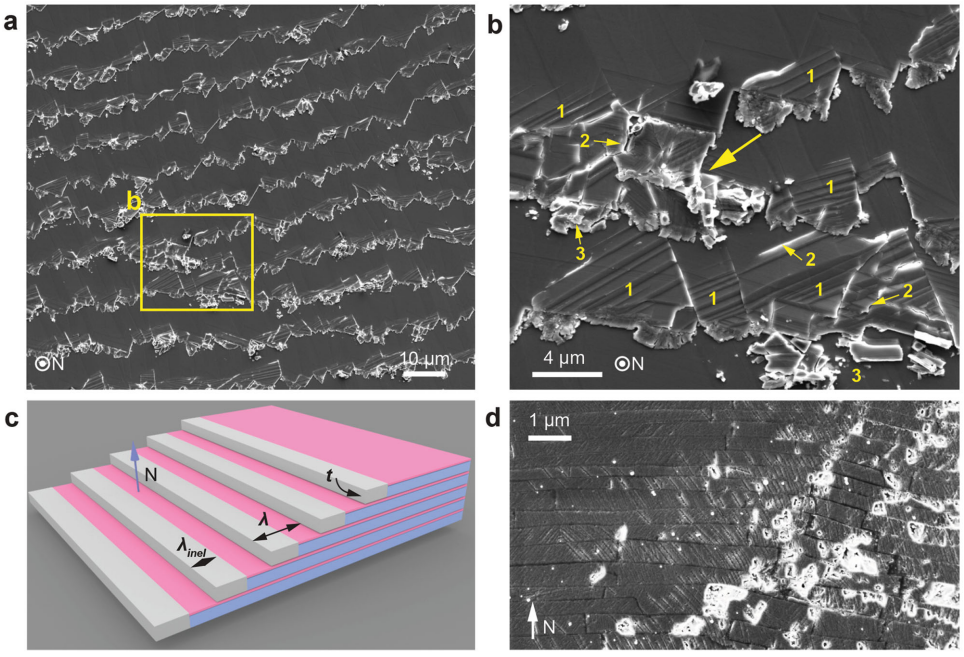

Figure 5. Microscopic deformation mechanisms activated by connection centers. a) SEM image of a fractured surface where the fractured interfaces have undergone extensive microscopic deformations. b) A high-magnification SEM image showing microscopic deformations surrounding a connection center (white arrow). Highlighted deformation modes include: (1) deformation twinning, (2) nano-/microcracking, and (3) fragmentation. c) Revised schematic diagram by including the microscopic inelastic deformation associated with individual fractured layers. d) Deformation twinning bands observed in a polished cross section of a macroindentation residue. Also note the rotation of mineral layers from their original orientations.

nanocracking, and fragmentation. The crack front fractured the mineral layers whenever it encountered connection centers. This led to the formation of an inelastic deformation zone at each layer, characterized by its width λ_{inel} (Figure 5c). As discussed above, bridging ligaments are formed when a crack encounters connection centers during propagation. A complex stress field is developed surrounding the vicinity of the connection centers, as evident from a finite element simulation analysis (Figure S5, Supporting Information). Local tensile and compressive stress fields facilitate microcracking and nanoscale deformation twinning, respectively, leading to enhanced energy dissipation.[31] The cross-sectional SEM image shown in Figure 5d also reveals a large number of deformation twinning bands within the damage zone.

2.3. Theoretical Analysis of Interfacial Fracture Toughness

By considering the primary involved energy dissipation terms, a simple theoretical analysis of interfacial fracture toughness, defined as the work dissipated in fracturing a unit interfacial area, can be formulated.[35] We compare two types of laminated composites: (1) a classic simple laminated structure without connection centers and (2) a modified laminated structure with connection centers.

For the simple laminated composite structure without connection centers, the interfacial fracture toughness is simply the interface energy between two adjacent mineral layers, i.e.

$$e_1 = e_{int} \tag{2}$$

where e_{int} is the interface energy between two adjacent mineral layers (J m^{-2}).

For the laminated composite structure with connection centers, extra energy is dissipated through three additional mechanisms: (1) inelastic deformation zone (λ_{inel}, Figure 5c), (2) extra vertical surfaces generated due to the fracture of mineral layers along the fracture lines, and (3) extra interface opening associated with inelastic deformation zone (see details in the Supporting Information). This can be represented as

$$e_2 = e_{int} + \frac{t\lambda_{inel}}{\lambda} e_{inel} + \frac{t}{\lambda} e_{cal} + \frac{\lambda_{inel}}{\lambda} e_{int} \tag{3}$$

where e_{inel} is the energy dissipation density of the mineral layers (J m^{-3}), e_{cal} is the surface energy along the cleavage plane of calcite (J m^{-2}), and t is the thickness of mineral layers (m).

By assuming $\lambda_{inel} \approx \lambda$ (Figure 5a,b), we can further approximate the interfacial fracture toughness of the laminated composite with connection centers as

$$e_2 = 2e_{int} + te_{inel} + \frac{t}{\lambda} e_{cal} \tag{4}$$

The magnitudes of the interfacial fracture toughness for the two composite structures can then be estimated by using previously reported values of e_{int}, e_{cal}, and e_{inel}. The interface energy between two adjacent mineral layers (e_{int}) is approximated as that of the nacreous structure (≈1 J m^{-2}),[36] and the surface energy of calcite crystal along a cleavage plane (e_{cal}) is ≈0.2 J m^{-2}.[37,38] The energy dissipation density of the

Table 1. Quantification of interface area generated in the damage zone and energy dissipation from indentation experiment.

Parameters	Sample 1	Sample 2	Sample 3
Total interface opening area generated [mm^2]	51.3	73.7	88.8
Interface energy, e_{int} [J m^{-2}]	1	1	1
Total energy dissipated by interface openings [mJ]	0.05	0.07	0.09
Total energy dissipated [mJ]	13.96	13.96	13.96
Percentage of energy dissipated via interface opening [%]	0.37	0.53	0.64

"Total interface opening area generated" was measured based on μ-CT data. Note this is an underestimation due to the resolution of the X-ray tomography technique (voxel size, 2.84 μm), and microcracks with spacing smaller than this value were not detected. "Interface energy," e_{int}, is taken from ref. [36]. "Total energy dissipated by interface openings" is obtained by multiplying "Total interface opening area generated" by "Interface energy." "Total energy dissipated" is the average value calculated by integrating the area under the load-displacement curves of macroindentation experiment (Figure 2c, $n = 7$).

calcitic mineral layers in *P. placenta* was previously determined to be $0.29 \pm 0.07 \times 10^9$ J m^{-3}.[31] The interfacial fracture toughness are then estimated as

$$e_1 = \approx 1 \text{ J m}^{-2}$$
$$e_2 = \approx 100 \text{ J m}^{-2} \quad (5)$$

Here we see that by incorporating the connection centers the highly mineralized shell of *P. placenta* is able to enhance the interface toughness by almost two orders of magnitude. Moreover, these numbers indicate that interface opening's contribution to total energy dissipation is ≈1%, which is consistent with previous studies on nacre.[36]

With the 3D information acquired from the μ-CT measurement, we can roughly estimate the total surface area generated through interface opening during one indentation cycle (50–90 mm^2, as shown in **Table 1**). We should note here that the accuracy of this estimation is limited by the resolution of the X-ray tomography technique, and microcracks with interfacial opening smaller than the voxel size (2.84 μm) were not detected, representing an underestimation of the actual total interface opening area. The total energy dissipation during one indentation cycle can be obtained by integrating the area under the indentation curves (≈14 mJ). Thus, the contribution from interface opening for the total energy dissipation can be calculated as 0.3%–0.6%. This value is slightly lower than the theoretical estimations above due to the underestimation of total interface opening area.

3. Discussion and Conclusion

A few studies previously reported out-of-plane interconnecting structures among adjacent mineral layers in some mollusk microstructures, for example, nanoscale mineral bridges[39] and similar screw dislocation-like structures in nacre.[32–34] The mineral bridges, due to their nanoscopic sizes, were suggested to play a marginal role in mechanical behavior.[40] The screw dislocation-like structures in nacre are believed primarily to provide biomineralization pathways for the formation of the nacreous structure.[32–34] These structures allow the spiral growth of the orderly lamellar nacre and maintain "levels of terraces of adjacent growth pyramids,"[32] which lead to the final closely packed lamellar structure. Yao et al. suggested that the connection centers in nacre might enhance nacre's strength by interlocking and resisting tablets' motion.[33] We argue that the screw dislocation-like connection centers in nacre do not contribute significantly to the interfacial fracture toughness in comparison to *P. placenta* shells. Due to the relatively small pseudo-hexagonal tablets in nacre (diameter, ≈5–10 μm), cracks can simply bypass the connection centers by fracturing along the vertical boundaries of tablets without any inelastic deformation of individual tablets. In this process, little extra energy is dissipated since the more efficient volumetric deformation mechanisms within mineral tablets are not activated. This argument is supported by many electron microscopic images of the fractured surfaces of nacre, which are usually characterized by smooth and sharp vertical fracture surfaces along the boundary of adjacent tablets and little plastic deformation within mineral tablets.[33,34,36]

Tablet pull-out has been identified as one of the key mechanisms responsible for the high toughness of nacre.[21,22,41,42] Theoretical analysis based on shear force transfer from a continuous soft polymer matrix to the stiff tablet suggests that the aspect ratio (s) between the lateral dimension and the vertical thickness plays a critical role in determining the strength and toughness of the composite.[27] Larger aspect ratios provide efficient load transfer to tablets and thus increase strength, while the fracture toughness may be reduced due to possible premature fracture of tablets. Therefore, aspect ratios slightly below the critical value, as determined by $s_{critical} = \sigma_f / \tau\gamma$, are considered to be optimal in providing both high strength and toughness. Indeed, structural measurements of various nacreous structures suggest a good agreement with this analysis.[43]

The estimated aspect ratio of the building blocks in *P. placenta* is ≈500 (length: ≈140 μm; thickness: ≈0.3 μm), which is more than an order of magnitude higher than the optimal value for the "pull-out" deformation mode ($s_{critical}$: ≈25; σ_f: ≈1 GPa; $\tau\gamma$: ≈40 MPa).[27] This indicates that, unlike nacre, tablet pull-out is probably not the primary toughening mechanism in *P. placenta* shells. Instead, the presence of screw dislocation-like connection centers within this laminated composite is able to activate a series of unique hierarchical energy dissipation processes spanning several length scales. Under high load indentation conditions, this biological composite is able to form an interconnected network of microcracks surrounding the damage zone while still maintaining the overall structural integrity. This interconnected network of microcracks is formed due to the crack deflection by connection centers. In addition, since the propagating cracks have to fracture the mineral layers whenever crossing connection centers, local multiaxial stress fields are generated around the vicinity of connection centers. This activates a series of microscopic deformation mechanisms, such as deformation twinning, nanocracking, fragmentation, grain formation and reorientation, and amorphization.[31] As suggested by both theoretical analysis and experiment-based calculations,

the activation of these nanoscopic volumetric energy dissipation mechanisms is able to boost the interfacial fracture toughness by ≈100 times in comparison to a conventional laminate architecture without connection centers. By judiciously incorporating this structure motif, the biological composite is able to directly bridge the macroscopic and nanoscopic deformation mechanisms for enhanced energy dissipation and damage resistance.

In-plane delamination failure along interfacial layers is one of the key problems of engineering laminated composite materials, which greatly affects the fracture energy dissipation and damage tolerance, particularly under out-of-plane impact loading conditions.[8,35,44] A number of interfacial control strategies have been proposed and developed to enhance the fracture toughness while still maintaining the out-of-plane strength. In particular, placing reinforcement structures along the out-of-plane direction of laminated composites, such as stitching fibers, steel wires, or whiskers, has been shown to improve the interfacial toughness and antidelamination performance.[6–8] However, addition of these vertical delamination antidelamination structures typically results in damage of the original laminated structure, entrapment of voids, and formation of stress concentration regions.[8] Recently, limited success has been demonstrated by growing interlaminar carbon nanotube forests to strengthen the laminates along the thickness direction.[11] Delamination is also one of the major obstacles of the efficient application of laminate-based transparent armor materials.[45] Reinforcement along the vertical direction with structures such as stitching fibers is simply impossible since most transparent protective materials are based on strong and brittle ceramics and glasses, for which drilling is not a good idea. Even if we succeeded in placing vertical reinforcement structures, optical transparency will certainly be compromised due to light scattering and/or absorption by the addition of secondary phases and generation of additional interfaces.

The screw dislocation-like connection centers discovered in this work provides an effective solution for minimizing delamination by forming the entire laminated structure as a 3D interconnected and integrated structure. Unlike stitching with additional fibers or wires in a discrete manner, this type of out-of-plane reinforcement minimizes local structural discontinuities and introduces little structural modification to the original laminated structure. In addition, this toughening mechanism relies primarily on the architectural design of the composite structure rather than on the intrinsic properties of constituents. With recent advancement in fabrication techniques, particularly additive manufacturing, this design principle can be potentially applied to fabricate improved laminated composite materials. Additionally, we believe this structural design principle is particularly relevant to transparent armor systems. With these connection centers, the antidelamination performance can be improved while still maintaining high optical transparency with minimal structural changes to its original laminate design.

In addition to enhancement of delamination resistance, incorporation of the screw dislocation-like connection centers also allows one to control the composite structure locally without introducing sharp discontinuities. One possible application is related to edge delamination, which is induced by the 3D interlaminar stresses developed at stress-free edges.[46] As shown in this work, the interfacial fracture toughness is directly related to the density of connection centers; therefore, it is possible to minimize edge delamination failure by placing more connection centers around edges. Another possible application of controlling the density and signs of connection centers is local thickness control. Currently, variation of local thickness in laminated composites is usually achieved by simply removing some of the layers in the area of thickness reduction, so-called ply drop-off.[44] This configuration produces interface discontinuities which can lead to delamination.[44] This problem can be potentially resolved by placing connection centers with specific signs so that local thickness can be controlled without generating sharp interface discontinuities.

4. Experimental Section

Samples: Edge-trimmed and intact *P. placenta* shells were purchased from Seashell World (Florida, USA) and Conchology, Inc. (Philippines), respectively. The specimens are stored in dry conditions prior experiments.

Instrumented Macroindentation: P. placenta shells were first cut into square-shaped samples (≈2 cm in size) with a diamond saw. The calcite samples for this test were prepared by cleaving a large calcite crystal into plate-shaped samples along easy cleavage planes. High load indentation experiments were performed on a Zwick Mechanical Tester (Zwick Z010, Zwick Roell, Germany), and the load-displacement curves were recorded. The indentation tip was a customized tungsten needle with a conical tip (full angle, ≈31°; tip radius, ≈0.1 mm; base diameter, 0.5 mm). All indentation experiments were under displacement control (displacement rate: 0.02 mm s^{-1}).

Electron Microscopy: Samples were coated with ultra-thin carbon prior SEM observations. Samples were imaged using Helios Nanolab 600 Dual Beam (FEI, OR) at the acceleration voltages of 2 and 5 kV and working distance of 4 mm.

Atomic Force Microscopy: Tapping mode AFM (TMAFM) imaging in ambient conditions was carried out using a Digital Instruments Multimode SPM IIIA (Veeco, Santa Barbara, CA) with an AS-130 "JV" scanner. TMAFM imaging was conducted with NANOSENSORS Si TMAFM cantilevers (PPP-NCHR-10). Typical scan speed was 1–5 μm s^{-1}, and other parameters were optimized upon tuning. The imaging modes include height (i.e., Z-piezo movement) and amplitude (i.e., cantilever oscillation amplitude).

X-Ray Micro-Computed Tomography: Pre-cut *P. placenta* shells (size, ≈3 mm) were first tested with macroindentation experiments as described above. Then the indented shells were scanned with an energy of 18 keV and a resolution of 2.84 μm $voxel^{-1}$ at beamline 2-BM of the Advanced Photon Source of Argonne National Laboratory. Mimics (Materialise, Belgium) was used for image segmentation and construction of 3D triangulated surface meshes (binary STL format). The surface area of the interface generated by the indentations was measured using netfabb (www.netfabb.com). For generation of 3D illustration and movie, STL meshes were directly imported into and rendered using Blender (www. blender.org).

Supporting Information

Supporting Information is available from the Wiley Online Library or from the author.

Acknowledgements

The authors gratefully acknowledge support of the National Science Foundation through MIT Center for Materials Science and Engineering (DMR-0819762) and the National Security Science and Engineering

Faculty Fellowship Program (N00244-09-1-0064). The authors thank Argonne National Laboratory for providing beamline time at 2BM at Advanced Photon Source and acknowledge the great assistance from Dr. Xianghui Xiao at the beamline. The authors would also like to thank Dr. Shiahn Chen and Dr. Matthew J. Connors for their technical assistance. The authors thank Prof. Jie Yin for providing the finite element simulation analysis. The authors would like to acknowledge Dr. James Weaver for helpful comments.

Received: January 29, 2015
Revised: March 16, 2015
Published online: May 4, 2015

[1] M. E. Launey, R. O. Ritchie, *Adv. Mater.* **2009**, *21*, 2103.
[2] R. O. Ritchie, *Nat. Mater.* **2011**, *10*, 817.
[3] K. K. Chawla, *Composite Materials: Science and Engineering*, Springer, New York **2001**.
[4] P. F. Becher, *J. Am. Ceram. Soc.* **1991**, *74*, 255.
[5] T.-W. Shyr, Y.-H. Pan, *Compos. Struct.* **2003**, *62*, 193.
[6] V. A. Guenon, T.-W. Cho, J. W. Cilliespie Jr., *J. Mater. Sci.* **1989**, *24*, 4168.
[7] W. C. Chung, B. Z. Jang, T. C. Chang, L. R. Hwang, R. C. Wilcox, *Mater. Sci. Eng. A* **1989**, *112*, 157.
[8] K. Dransfield, C. Baillie, Y. Mai, *Compos. Sci. Technol.* **2006**, *50*, 305.
[9] A. P. Mouritz, M. K. Bannister, P. J. Falzon, K. H. Leong, *Compos. Part A: Appl. Sci. Manuf.* **1999**, *30*, 1445.
[10] L. Tong, A. P. Mouritz, M. K. Bannister, *3D Fibre Reinforced Polymer Composites*, Elsevier, Kidlington, OX, UK **2002**.
[11] V. P. Veedu, A. Cao, X. Li, K. Ma, C. Soldano, S. Kar, P. M. Ajayan, M. N. Ghasemi-Nejhad, *Nat. Mater.* **2006**, *5*, 457.
[12] A. R. Studart, *Adv. Mater.* **2012**, *24*, 5024.
[13] J. W. C. Dunlop, P. Fratzl, *Annu. Rev. Mater. Res.* **2010**, *40*, 1.
[14] M. A. Meyers, P.-Y. Chen, A. Y. -M. Lin, Y. Seki, *Prog. Mater. Sci.* **2008**, *53*, 1.
[15] C. Ortiz, M. C. Boyce, *Science* **2008**, *319*, 1053.
[16] A. Miserez, J. C. Weaver, P. J. Thurner, J. Aizenberg, Y. Dauphin, P. Fratzl, D. E. Morse, F. W. Zok, *Adv. Funct. Mater.* **2008**, *18*, 1241.
[17] R. Wang, H. S. Gupta, *Annu. Rev. Mater. Res.* **2011**, *41*, 41.
[18] D. F. Schmidt, *Mater. Lett.* **2013**, *108*, 328.
[19] J. D. Currey, *Proc. R. Soc. London B* **1977**, *196*, 443.
[20] J. D. Currey, J. D. Taylor, *J. Zool.* **1974**, *173*, 395.
[21] F. Barthelat, H. D. Espinosa, *Exp. Mech.* **2007**, *47*, 311.
[22] F. Barthelat, H. Tang, P. Zavattieri, C. Li, H. Espinosa, *J. Mech. Phys. Solids* **2007**, *55*, 306.
[23] M. A. Meyers, P. Chen, M. I. Lopez, Y. Seki, A. Y. M. Lin, *J. Mech. Behav. Biomed. Mater.* **2011**, *4*, 626.
[24] P.-Y. Chen, A. Y. M. Lin, Y. S. Lin, Y. Seki, A. G. Stokes, J. Peyras, E. A. Olevsky, M. A. Meyers, J. McKittrick, *J. Mech. Behav. Biomed. Mater.* **2008**, *1*, 208.
[25] G. Mayer, M. Sarikaya, *Exp. Mech.* **2002**, *42*, 395.
[26] B. Ji, H. Gao, *J. Mech. Phys. Solids* **2004**, *52*, 1963.
[27] H. Gao, B. Ji, I. L. Ja, E. Arzt, P. Fratzl, *Proc. Natl. Acad. Sci. U. S. A.* **2003**, *100*, 5597.
[28] H. D. Espinosa, A. L. Juster, F. J. Latourte, O. Y. Loh, D. Gregoire, P. D. Zavattieri, *Nat. Commun.* **2011**, *2*, 173.
[29] F. Bouville, E. Maire, S. Meille, B. Van de Moortèle, A. J. Stevenson, S. Deville, *Nat. Mater.* **2014**, *13*, 508.
[30] L. Li, C. Ortiz, *Adv. Mater.* **2013**, *25*, 2344.
[31] L. Li, C. Ortiz, *Nat. Mater.* **2014**, *13*, 501.
[32] S. W. Wise, J. DeVilliers, *Trans. Am. Microsc. Soc.* **1971**, *90*, 376.
[33] N. Yao, A. Epstein, A. Akey, *J. Mater. Res.* **2006**, *21*, 1939.
[34] N. Yao, A. K. Epstein, W. W. Liu, F. Sauer, N. Yang, *J. R. Soc. Interface* **2009**, *6*, 367.
[35] J.-K. Kim, Y.-W. Mai, *Compos. Sci. Technol.* **2006**, *41*, 333.
[36] A. K. Dastjerdi, R. Rabiei, F. Barthelat, *J. Mech. Behav. Biomed. Mater.* **2013**, *19*, 50.
[37] M. Bruno, F. R. Massaro, M. Prencipe, *Surf. Sci.* **2008**, *602*, 2774.
[38] M. Bruno, F. R. Massaro, M. Rubbo, M. Prencipe, D. Aquilano, *Cryst. Growth Des.* **2010**, *10*, 3102.
[39] A. G. Checa, J. H. E. Cartwright, M.-G. Willinger, *J. Struct. Biol.* **2011**, *176*, 330.
[40] K. S. Katti, D. R. Katti, S. M. Pradhan, A. Bhosle, *J. Mater. Res.* **2011**, *20*, 1097.
[41] L. J. Bonderer, A. R. Studart, L. Gauckler, *J. Sci.* **2008**, *319*, 1069.
[42] R. Rabiei, S. Bekah, F. Barthelat, *Acta Biomater.* **2010**, *6*, 4081.
[43] F. D. Fleischli, M. Dietiker, C. Borgia, R. Spolenak, *Acta Biomater.* **2008**, *4*, 1694.
[44] N. Sela, O. Ishai, *Composites* **1989**, *20*, 423.
[45] M. Grujicic, W. C. Bell, B. Pandurangan, *Mater. Des.* **2012**, *34*, 808.
[46] D. S. Balint, J. W. Hutchinson, *J. Appl. Mech.* **2001**, *68*, 725.